Nonlinear Smooth Orthogonal Decomposition of Kinematic Features of Sawing Reconstructs Muscle Fatigue Evolution as Indicated by Electromyography

David B. Segala
Nonlinear Dynamics Laboratory,
Department of Mechanical, Industrial and Systems Engineering,
University of Rhode Island,
Kingston, RI 02881

Deanna H. Gates
Department of Biomedical Engineering,
University of Texas at Austin,
Austin, TX 78712

Jonathan B. Dingwell
Nonlinear Biodynamics Laboratory,
Department of Kinesiology and Health Education,
University of Texas at Austin,
Austin, TX 78712

David Chelidze[1]
Nonlinear Dynamics Laboratory,
Department of Mechanical, Industrial and Systems Engineering,
University of Rhode Island,
Kingston, RI 02881
e-mail: chelidze@egr.uri.edu

Tracking or predicting physiological fatigue is important for developing more robust training protocols and better energy supplements and/or reducing muscle injuries. Current methodologies are usually impractical and/or invasive and may not be realizable outside of laboratory settings. It was recently demonstrated that smooth orthogonal decomposition (SOD) of phase space warping (PSW) features of motion kinematics can identify fatigue in individual muscle groups. We hypothesize that a nonlinear extension of SOD will identify more optimal fatigue coordinates and provide a lower-dimensional reconstruction of local fatigue dynamics than the linear SOD. Both linear and nonlinear SODs were applied to PSW features estimated from measured kinematics to reconstruct muscle fatigue dynamics in subjects performing a sawing motion. Ten healthy young right-handed subjects pushed a weighted handle back and forth until voluntary exhaustion. Three sets of joint kinematic angles were measured from the right upper extremity in addition to surface electromyography (EMG) recordings. The SOD coordinates of kinematic PSW features were compared against independently measured fatigue markers (i.e., mean and median EMG spectrum frequencies of individual muscle groups). This comparison was based on a least-squares linear fit of a fixed number of the dominant SOD coordinates to the appropriate local fatigue markers. Between subject variability showed that at most four to five nonlinear SOD coordinates were needed to reconstruct fatigue in local muscle groups, while on average 15 coordinates were needed for the linear SOD. Thus, the nonlinear coordinates provided a one-order-of-magnitude improvement over the linear ones. [DOI: 10.1115/1.4003320]

1 Introduction

Muscle fatigue is defined as a decrease in the force generating capacity of a muscle or muscle group after activity [1–3]. Due to the complexities in human muscular and physiological systems, deriving first principles models of muscle fatigue accumulation is a very complex problem. Therefore, numerous studies have focused on methods of tracking and predicting muscle fatigue accumulation. Tracking systemic (i.e., global) fatigue or local muscle fatigue requires invasive and/or impractical procedures that may not be realizable outside the laboratory. A few fatigue tracking methods that require invasive procedures and/or cumbersome sensing can be found in Refs. [4–6]. Several physiological fatigue markers can be obtained from oxygen consumption, onset of blood lactate, and *electromyography* (EMG) [5,6]. EMG has played a pivotal role as an indicator of local muscle fatigue and has been used in many tracking methodologies [2,4,7–10].

The use of surface EMG has been explored extensively in trying to quantify changes in muscle function in fatigue [11]. Fatigue is a combination of both central and peripheral processes [3]. At the peripheral level, there is a loss of force generating capacity of individual motor units [12]. To maintain force, the central nervous system can increase its drive to the muscles. This causes already active motor units to fire more frequently and causes larger motor units to be recruited. This leads to an increased sense of effort [3]. As fatigue progresses, the number of active motor units decreases, the muscle fiber conduction velocity decreases [13], the motor units fire more slowly [1], and the motor units become more synchronized [14]. These changes lead to decreases in the mean frequency (MNF) or the median frequency (MDF) of the EMG signal [1] and eventually to task failure [15]. To this extent, mean and median frequencies have served as good indicators of local muscle fatigue. Torvik et al. [4] examined several predictive measures (data mining, neural networks, and nearest-neighbor approaches) to try to track muscle fatigue through EMG. Also, "short-time" Fourier transform methods have been developed [9] and subsequently validated [7,8], which can track slowly varying changes in muscle fatigue across multiple dynamic contractions.

The concept of *phase space warping* (PSW) [16]—describing deformation in the phase space due to drifts in a dynamical system's parameters—was first used in the field of biomechanics by Dingwell et al. [17]. In particular, the slowly varying inclination angle of a treadmill was extracted using only kinematic time series for ten subjects walking at their preferred steady speed. *Smooth orthogonal decomposition* (SOD) was originally applied to multivariate PSW features to extract deterministic (smooth) trends from noisy PSW feature space [18]. SOD can be viewed as an extension of *proper orthogonal decomposition* (POD) [19], where not only spatial (i.e., statistical) but also temporal (i.e., dynamical) characteristics of the data are considered. In particular, SOD identifies coordinates that have both minimal temporal roughness and maximal spatial variance [19]. Further application of the PSW and SOD methodologies to stationary cyclists showed that fatigue information present in the standard EMG analysis was

[1]Corresponding author.

Contributed by the Bioengineering Division of ASME for publication in the JOURNAL OF BIOMECHANICAL ENGINEERING. Manuscript received July 14, 2010; final manuscript received December 2, 2010; accepted manuscript posted December 22, 2010; published online February 8, 2011. Editor: Michael Sacks.

also fully represented in the SOD coordinates extracted from the PSW features of cycling kinematics [20].

The SOD coordinates of kinematic PSW features can also adequately track an average oxygen consumption rate $\dot{V}O_2$ in load carrying soldiers, as shown in Refs. [21,22]. Furthermore, these same coordinates also reconstruct muscle fatigue as indicated by EMG-based markers in both the load carrying soldiers [23] and the sawing subjects [22]. In these studies, it was found that approximately 10–15 coordinates or 10- to 15-dimensional manifolds are needed to reconstruct both local and global (systemic) fatigue dynamics. However, lower-dimensional reconstructions of fatigue dynamics are still desired.

The work presented here is a natural extension of the PSW and *linear* SOD-based methodologies for reconstructing physiological fatigue dynamics from noninvasive biomechanical variables. The objective of this study was to further reduce the number of dimensions needed to reconstruct the fatigue dynamics. This was accomplished by three modifications to the PSW/SOD methodology: (1) A new weighting function was used for the PSW feature estimation, (2) SOD was applied to the nonlinear (i.e., polynomial) expansion of the original SOD coordinates, and (3) an ad hoc F test was used to statistically determine the number of SOD coordinates needed to reconstruct muscle fatigue. The modified methodology was tested on new experimental data of biomechanical (kinematic) variables, which were collected from subjects performing a sawing motion in a restrained position until voluntary exhaustion. Nonlinear SOD (NSOD) coordinates of PSW features were compared against independently measured fatigue markers (i.e., mean and median EMG spectrum frequencies of individual muscle groups).

2 Muscle Fatigue Identification Procedure

Similar to material damage in Refs. [16,17,24], muscle fatigue is viewed evolving in a hierarchical dynamical system where slow-time fatigue and fast-time motion dynamics are coupled through parameters of a fast-time subsystem,

$$\dot{x} = f(x, \mu(\phi), t), \quad \dot{\phi} = \varepsilon g(\phi, x), \quad \text{and} \quad y = h(x) \tag{1}$$

where $x \in \mathbb{R}^n$ is a fast-time dynamic variable describing sawing kinematics (directly observable), $\phi \in \mathbb{R}^m$ is a slow-time dynamic variable describing muscle fatigue evolution (assumed hidden), which alters a parameter vector μ in the fast-time system, t is time, and ε is a small positive rate constant describing time scale separation. A scalar measurement function h generating a scalar time series y is based on the fast-time variable, x.

2.1 Short-Time PSW-Based Features. The concept of PSW refers to deformations in the fast-time phase space trajectories due to underlying slow-time parameter drifts. Fast-time phase space trajectories are reconstructed from the scalar time series $\{y_i\}_{i=1}^{N} \in \mathbb{R}^d$ $(d \geq n)$ using delay coordinate embedding [25]. A d-dimensional state vector representing the reconstructed phase space is given by

$$y(i) = [y_i, y_{i-\tau}, \ldots, y_{i-(d-1)\tau}]^T \tag{2}$$

where T represents matrix transpose, d is a sufficient *embedding dimension*, and τ is a *delay time*. The embedding dimension is usually estimated by the method of false nearest neighbors [26], and the discrete time delay is estimated as the first local minimum of the average mutual information [27]. The reconstructed time series are split into N_r data records where the first data record is our reference data reflecting an unfatigued state.

It is assumed that the evolution of a point in the reconstructed phase space is governed by an unknown deterministic map, $P: \mathbb{R}^d \to \mathbb{R}^d$,

$$y(i+1) = P(y(i); \phi) \tag{3}$$

A simple *PSW tracking function* that describes the deformation of a trajectory for a point $y(i)$ in the reconstructed phase space is

$$e_R(y(i); \phi) = P(y(i); \phi) - P(y(i); \phi_R) \tag{4}$$

where ϕ_R is the reference (unfatigued) state of the fatigue variable and ϕ is the current (fatigued) state. We can rewrite Eq. (4) using Eq. (3) as

$$e_R(y(i); \phi) = y(i+1) - P(y(i); \phi_R) \tag{5}$$

since the value of $y(i+1) = P(y(i); \phi)$ is known from the current phase space reconstruction. Usually, there is no exact image of $y(i)$—or of its corresponding future state—in the reference reconstructed phase space; however, the map $y(i+1; \phi_R) = P(y(i); \phi_R)$ can be approximated by a reference local linear model. The estimation details of this model can be found in Refs. [16,17,24], so we only state the final result. In particular, the local linear model

$$P(y(i); \phi_R) \approx A_i y(i) + b_i \tag{6}$$

is estimated for each point $y(i)$ by finding its $\mathcal{Y}_i \equiv \{y^r(i; \phi_R)\}_{r=1}^{N_m}$ nearest neighbors in the reference data set and their images, $\mathcal{Y}_{i+1} \equiv \{y^r(i+1; \phi_R)\}_{r=1}^{N_m}$, one time step later. The local linear model parameter matrix $A_i \in \mathbb{R}^{d \times d}$ and a parameter vector $b_i \in \mathbb{R}^d$ are estimated from the reference set of points $\mathcal{Y}_i$ and $\mathcal{Y}_{i+1}$ in the least-squares sense. Thus, the tracking function is estimated using this *single-time-step reference model prediction* (STRMP) error,

$$\hat{e}_R(y(i); \phi) = y(i+1) - A_i y(i) - b_i \tag{7}$$

Since the drifts in the fast-time subsystem parameters alter the dynamics, the probability distribution of points in each data record will also be different. In addition, the accuracy of the local linear model will change as a function of the probability density in the reference data record—i.e., more densely populated regions will produce better and more accurate models. To overcome some of these pitfalls, the reference data record is partitioned into N_e disjoint hyperboxes $\{\mathcal{B}_i\}_{i=1}^{N_e}$ that contain approximately the same number of reference data points. Then, a weighted average STRMP error is estimated in each of these hyperboxes,

$$e_i(\phi) = \frac{\sum_{y \in \mathcal{B}_i} w(y) \| \hat{e}_R(y; \phi) \|}{\sum_{y \in \mathcal{B}_i} w(y)} \tag{8}$$

where the weight function $w(y) = w(y; \phi_R)$ accounts for the accuracy of reference local linear models used in the estimation and is explained below. Now, for each data record $j (j = 1, \ldots, N_r)$, these averaged errors are assembled into an N_e-dimensional *feature vector*,

$$e^j = [e_1(\phi), e_2(\phi), \ldots, e_{N_e}(\phi)] \tag{9}$$

The estimated feature vectors e^j are then calculated for all N_r data records and *row-wise* concatenated (in time sequence) into a vector-valued time series,

$$Y = [e^1, e^2, \ldots, e^{N_r}] \tag{10}$$

where $Y \in \mathbb{R}^{N_r \times N_e}$. We assume that the slow-time fatigue information is embedded in this feature space points estimated from only the measured fast-time dynamic variable.

2.1.1 Weighting Function for the STRMP Error. The probability density of points in the reference phase space will generally vary spatially. This is especially true for a nominally chaotic reference state, where the density function is generally fractal. As mentioned above, the accuracy of reference local linear models will be a function of this density—denser regions will have more accurate models. Thus, the accuracy of the STRMP error estimates $\hat{e}_R(y; \phi)$ will also be a function of the reference probability density near each point y. The weight function $w(y)$ in Eq. (8) is used to mitigate this source of noise. In this paper, a cloud of reference points $\mathcal{Y}_{i+1}$ (as used in estimating the corresponding

Table 1 Basic characteristics for each sawing subject

Subject number	Gender (M/F)	Age (yr)	Body mass (kg)	Weight applied (kg)	Metronome (bpm)	Time to failure (s)
1	F	28	55.0	4.54	133	850.63
2	M	26	71.2	7.37	128	644.13
3	M	32	95.5	9.07	123	1503.90
4	M	29	110.5	6.80	123	1858.60
5	F	30	62.5	3.40	133	905.30
6	M	26	61.5	5.67	131	1557.40
7	F	29	51.5	3.40	129	357.28
8	M	28	70.0	5.67	126	2472.20
9	F	26	70.0	5.67	131	2272.90
10	M	25	76.2	6.01	126	1341.30
Mean ± SD	–	27 ± 2	72.4 ± 18.2	5.67 ± 1.74	128 ± 4	1376.36 ± 696.06

reference local linear model) is used to determine appropriate weighting. In the weighting, we account for three factors contributing to the accuracy of prediction: (1) the relative size of a cloud of reference nearest neighbors $\mathcal{Y}^{i+1}$, (2) the shape of this cloud, and (3) its orientation with respect to the STRMP error. These three factors are determined using singular value decomposition of the matrix containing all the points in $\mathcal{Y}^{i+1}$ (with mean subtracted from each coordinate). The resulting weighting function is given as

$$w(y) = e^{-r_s(y)}(\sin\ \theta(y))^{[1-r_\sigma^2(y)]} \tag{11}$$

where

$$r_\sigma(y) = \frac{\sigma_2(y)}{\sigma_1(y)}, \quad r_s(y) = \frac{\sigma_1(y)}{\|\hat{e}_R(y;\phi)\|}, \quad \theta(y) = \measuredangle\,(s_1(y), \hat{e}_R(y;\phi)) \tag{12}$$

and for $y=y(i)$ point, $\sigma_1(y)$ and $\sigma_2(y)$ are the first two largest singular values of the corresponding cloud of reference points $\mathcal{Y}_{i+1}$, and $s_1(y)$ is the singular vector corresponding to the largest singular value. Using Eq. (11) in Eq. (8), in addition to the size of a cloud $\mathcal{Y}_{i+1}$, we account both for the degree of elongation of the cloud and the alignment of that elongation along the corresponding STRMP error. Thus, in Eq. (8), we weight heavier STRMP errors that have the smallest spread of the cloud along their direction. It was found that this weighting provided noticeable improvement over the uniform weighting used previously. These results will be published separately and are not included here for brevity.

3 Smooth Orthogonal Decomposition

As mentioned before, SOD can be viewed as an extension of POD, where not only spatial (i.e., statistical) but also temporal (i.e., dynamical) characteristics of the data are considered [19]. We assume that muscle fatigue is a deterministic process evolving smoothly in time. It is hypothesized that if the multivariate PSW feature time series Y contain information about this fatigue, SOD should be able to extract smooth coordinates that correlate with it. In general, SOD is determined by solving the following generalized eigenvalue problem:

$$\Sigma_Y \psi_i = \lambda_i \Sigma_{DY} \psi_i \tag{13}$$

where

$$\Sigma_Y = \frac{1}{N-1} Y^T Y \quad \text{and} \quad \Sigma_{DY} = \frac{1}{N-1} Y^T D^T D Y \tag{14}$$

are auto-covariance matrices of Y and DY, where D is some discrete differential operator (e.g., based on forward difference) and superscript T represents a matrix transpose. In practice, Eq. (13) is solved using *generalized singular value decomposition* of the matrix pair Y and DY. λ_i are generalized eigenvalues or *smooth orthogonal values* (SOVs) and ψ_i are the generalized eigenvectors or *smooth projection modes* (SPMs). By projecting our matrix Y onto the SPMs, we obtain *smooth orthogonal coordinates* (SOCs),

$$q_i = Y\psi_i \tag{15}$$

whose smoothness is described by the magnitude of the corresponding SOVs. The greater the magnitude of the SOV, the smoother in time is its corresponding SOC.

3.1 Nonlinear Extension of Smooth Orthogonal Decomposition. The nonlinear extension refers to the inclusion of nonlinear combinations of the original features in the SOD analysis. In this paper, to limit the unnecessary expansion of the nonlinear feature space, the second- and third-order NSODs are considered using polynomial expansions of only the dominant SOCs—Eq. (15), $\{q_i\}_{i=1}^{p}$. Dominant p SOCs are identified during the original linear SOD analysis by the dominant SOVs. A new vector-valued time series representing the second-order Taylor series expansion of the linear SOCs is obtained,

$$Y^{(2)} = [[q_1, \ldots, q_p], [q_1 \cdot q_1, q_1 \cdot q_2, \ldots, q_1 \cdot q_p, \ldots, q_p \cdot q_p]] \tag{16}$$

where $\cdot$ indicates term-by-term multiplication of the arrays. Similarly, the cubic expansion is obtained as

$$Y^{(3)} = [Y^{(2)}, [q_1 \cdot q_1 \cdot q_1, q_1 \cdot q_1 \cdot q_2, \ldots, q_1 \cdot q_1 \cdot q_p, \ldots, q_p \cdot q_p \cdot q_p]] \tag{17}$$

Nonlinear SOCs (NSOCs) $q_i^{(o)}$ can now be obtained by linear SOD of this new multivariate time series in Eq. (17) or through generalized singular value decomposition of the corresponding matrices $Y^{(o)}$ and $DY^{(o)}$, where $o=2$ or 3.

4 Experimental Design and Data Analysis

Ten healthy right-handed subjects (six male and four female) participated (Table 1). All participants signed institutionally approved consent forms and were screened to ensure that no subject had a history of medications, surgeries, injuries, or illnesses that might have affected their upper extremity joint movements. Subjects sat in an adjustable chair with seatbelts to help them maintain a constant posture. They then pushed a weight back and forth along a low friction horizontal track in time with a metronome (~1 Hz, the exact frequency for each subject was determined based on their own estimated body mass) until voluntary exhaustion (refer to Ref. [28] for additional details). Kinematic and EMG data were collected continuously throughout the trial. To ensure that the task resistance was comparable across subjects, each subject's maximum pushing/pulling force was measured using a second custom handle attached to a Baseline® dynamometer that was rigidly mounted on a table. Subjects alternately pushed and then pulled on this rigidly fixed handle with maximal effort three times

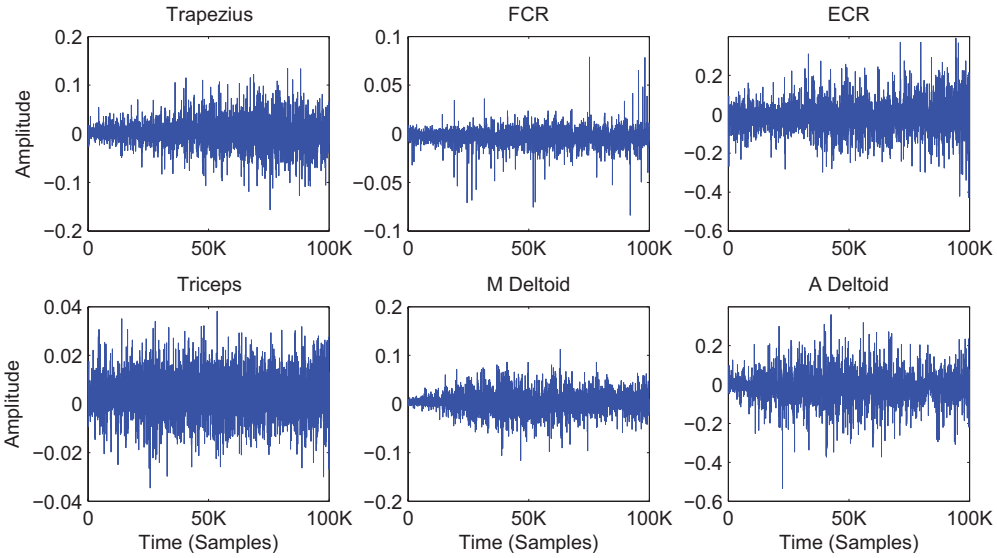

Fig. 1 Recorded raw EMG time series for subject 6

for 5 s each time, with at least 60 s of rest in between each attempt. The average of these six peak forces applied during each maximal effort defined the subject's maximum isometric pushing/pulling strength (MPS). This was used to set a target resistance of 15% MPS for each task. This percent was chosen from pilot testing to achieve complete fatigue in approximately 15–20 min for most subjects. Due to equipment limitations, if the subject was not fatigued after 45 min, they were excluded from the study.

4.1 Kinematic Data Capturing. Nineteen reflective markers were placed on the arm and trunk to define the movements of four body segments. Markers were placed on the trunk at the right and left acromium processes and sternal notch. Clusters of four markers were placed on the upper and lower arms to define the segments. The hand was defined by four markers at the ulnar epicondyles of the wrist and third and fifth metacarpal-phalangeal (MCP) joints. Additional markers were placed on the medial and lateral humeral epicondyles for a static calibration trial. One additional marker was placed on the top of the handle to define the beginning and end of each cycle. The three-dimensional movements of these markers were recorded continuously during all trials at 60 Hz using an eight-camera Vicon-612 motion analysis system (Oxford Metrics, Oxford, UK). Marker data were filtered using a fifth-order Butterworth filter with a cutoff frequency of 15 Hz. Segment coordinate systems were calculated based on the marker positions with a least-squares algorithm [29]. The joint centers at each instant in time were then calculated based on the position of the joint markers during the static trial (Schmidt et al. [30]). Local coordinate systems were then defined using the International Society of Biomechanics' (ISB) recommendations for the humerus and forearm [31] and a modified coordinate system for the trunk [32] and wrist [33]. The three-dimensional movements of the right arm were determined using Euler rotations in accordance with ISB recommendations [31]. Three sets of angles were measured from the shoulder (humeral plane, elevation, and rotation), elbow (flexion/extension, pronation/supination, and carrying angle, essentially zero), and wrist (flexion/extension, ulnar/radial deviation, and pronation/supination).

4.2 EMG Data Capturing. Nine preamplified EMG surface electrodes (Delsys Inc., Boston, MA) were attached to the right arm and torso to record activity in nine muscles: flexor carpi radialis, extensor carpi radialis longus, biceps, triceps (lateral head), deltoid (anterior, lateral, and posterior), middle trapezius, and pectoralis major. Electrodes were positioned over each muscle according to accepted recommendations [34]. EMG signals were recorded at 1080 Hz using a Delsys Bagnoli-8 system integrated with the Vicon-612 system. Data were filtered to a bandwidth between 20 Hz and 450 Hz. From here, MNF and MDF were calculated from the EMG power spectrum. MNF and MDF cannot be calculated straight from the unfiltered time series (as shown in Fig. 1). EMG goes through cycles of accumulation and relief. The entire time series is considered nonstationary over these regions of accumulation and relief [34]. Time points defining the beginning, middle, and end of each cycle, as determined from the marker data, were used to split each EMG signal into the push and pull strokes. Mean and median power frequencies (MNF and MDF) of the EMG signals were used to indicate muscle fatigue [2]. The MNF and MDF for each stroke (either push or pull) were computed from the power spectrum of the signal using Welch's method (MATLAB, Mathworks, Natick, MA). The MNF and MDF for each complete movement cycle (push plus pull) were calculated as the average of the MNFs and MDFs for the push and pull strokes [9]. It has been shown that as a muscle fatigues, the bandwidth of the EMG spectrum tends toward lower frequencies [10]. To this end, fatigued muscles should show a decrease in the mean and/or median frequency of the power spectrum.

5 Results

Out of ten subjects, three subjects (numbers 1, 4, and 5) were not included in the results presented here. This decision was based on two criteria: (1) if the middle and anterior deltiod muscles did not show a decrease of at least 20% from the percentage of the initial value in the mean frequency spectrum and (2) if there was a limited dynamical structure in the kinematics when plotting with the time delay. For a kinematic analysis, particulars about the data processing will be described for the elbow flexion/extension angle of subject 6, which showed middle of the line results. The time delay and embedding dimension were found to be 21 and 3, respectively. The kinematic time series had 53,442 points, and the EMG had 961,953 points. The reference phase space was spilt into 32 hyperboxes, and the local linear model was based on 16 nearest neighbors in the reference data.

Figure 1 shows the raw EMG data for subject 6. Since the EMG is nonstationary across multiple cycles of accumulation and relief, the EMG time series must be preprocessed first just like in Ref. [28]. The EMG time series was split into regions of one complete stroke. Across this complete cycle of push and pull, the time series is assumed to be stationary. Figure 2 depicts the new time series for both MNF (blue line) and MDF (red line) with 966 complete

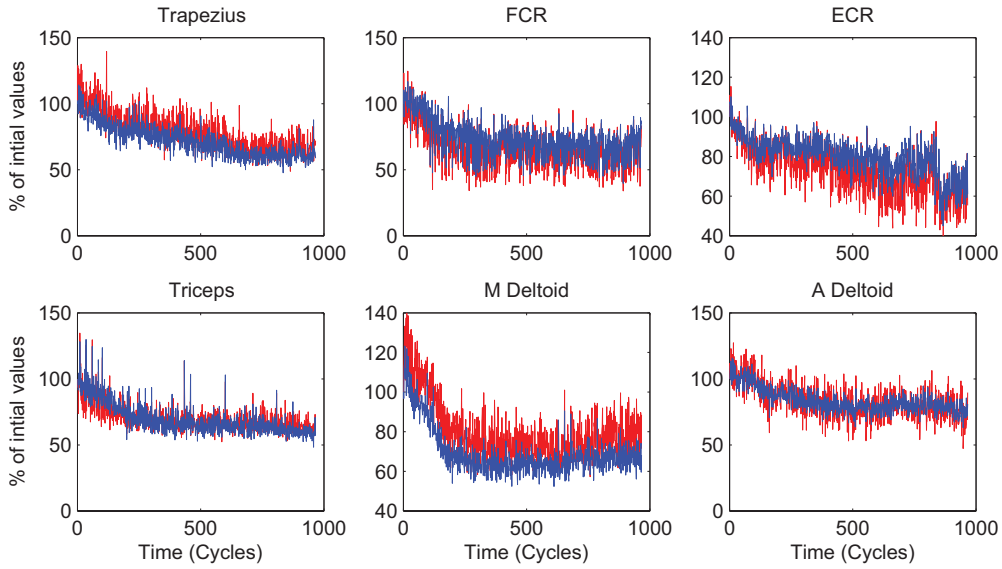

Fig. 2 MNF (darker line) and MDF (lighter line) calculated over individual cycles of EMG data of subject 6

cycles (points). Figure 3 shows the final averaged MDF and MNF curves whose length (60 points) matches the length of SOCs calculated for this particular subject.

SOVs of kinematic PSW features can be seen in left plots of Fig. 4 for elbow flexion/extension (top plots), humeral plain angle (middle plots), and humeral elevation angle (bottom plots). In all three plots, on average, only two SOVs are observed to be distinctly separated from the rest in the linear SOD analysis. However, some additional slow-time information could leak into higher-order linear modes. Therefore, five linear SOCs were used in the NSOD analysis for both quadratic and cubic expansions. This reduction in linear modes used was necessitated by the drastic growth of the total number of nonlinear modes with the increase in the basis linear mode numbers. The number of linear modes retained was consistent across all angles and subjects for the NSOD analysis.

Figure 4 depicts results from both linear and nonlinear (quadratic and cubic expansions) SOD analyses of the elbow flexion/extension, humeral plane angle, and humeral elevation angle PSW features. Only the first 15 SOVs are shown in Fig. 4 with the corresponding four most dominant smooth coordinates (SOCs). From SOV plots, it is clear that the nonlinear analysis provides SOVs that are greater in magnitude then their linear counterparts, cubic SOVs being the largest. This can also be seen in the corresponding smooth coordinates, where the nonlinear coordinates in all three figures are smoother than the corresponding linear coordinates, cubic coordinates showing considerably smoother trends. Referring to Fig. 4, there is a clear separation between the first one or two dominant SOVs and the point where the values start falling off to the noise floor (indicating high frequency contamination). This is clearly seen in the corresponding smooth coordinates also: As the SOC index increases, more high frequency content is present.

The coefficient of determination, R^2, values are used to determine how well SOC-based fits match the actual EMG-based fatigue markers. For each set of SOCs, monotonically increasing number of SOCs are projected onto MNF and MDF trends in the

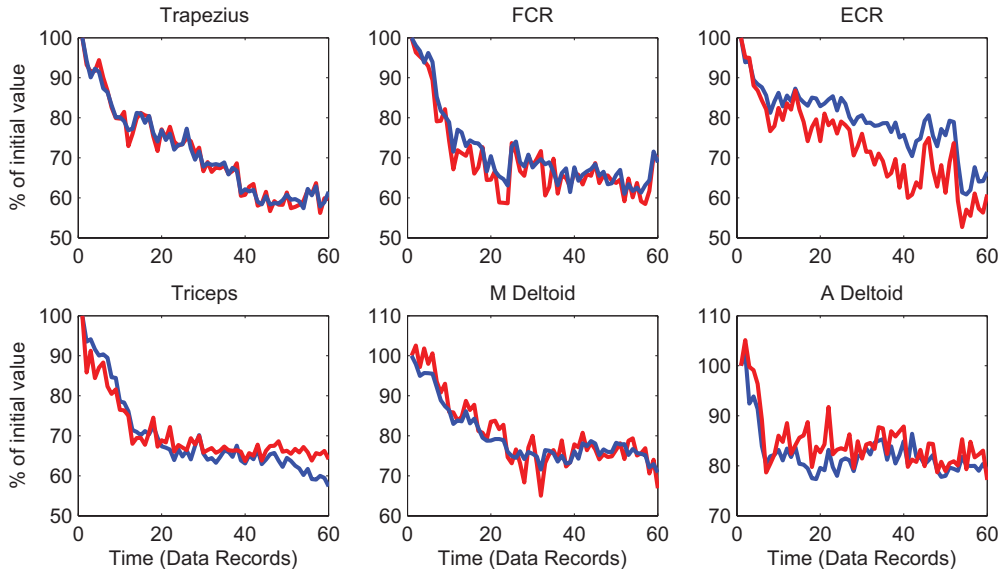

Fig. 3 Averaged MNF (darker line) and MDF (lighter line) for subject 6

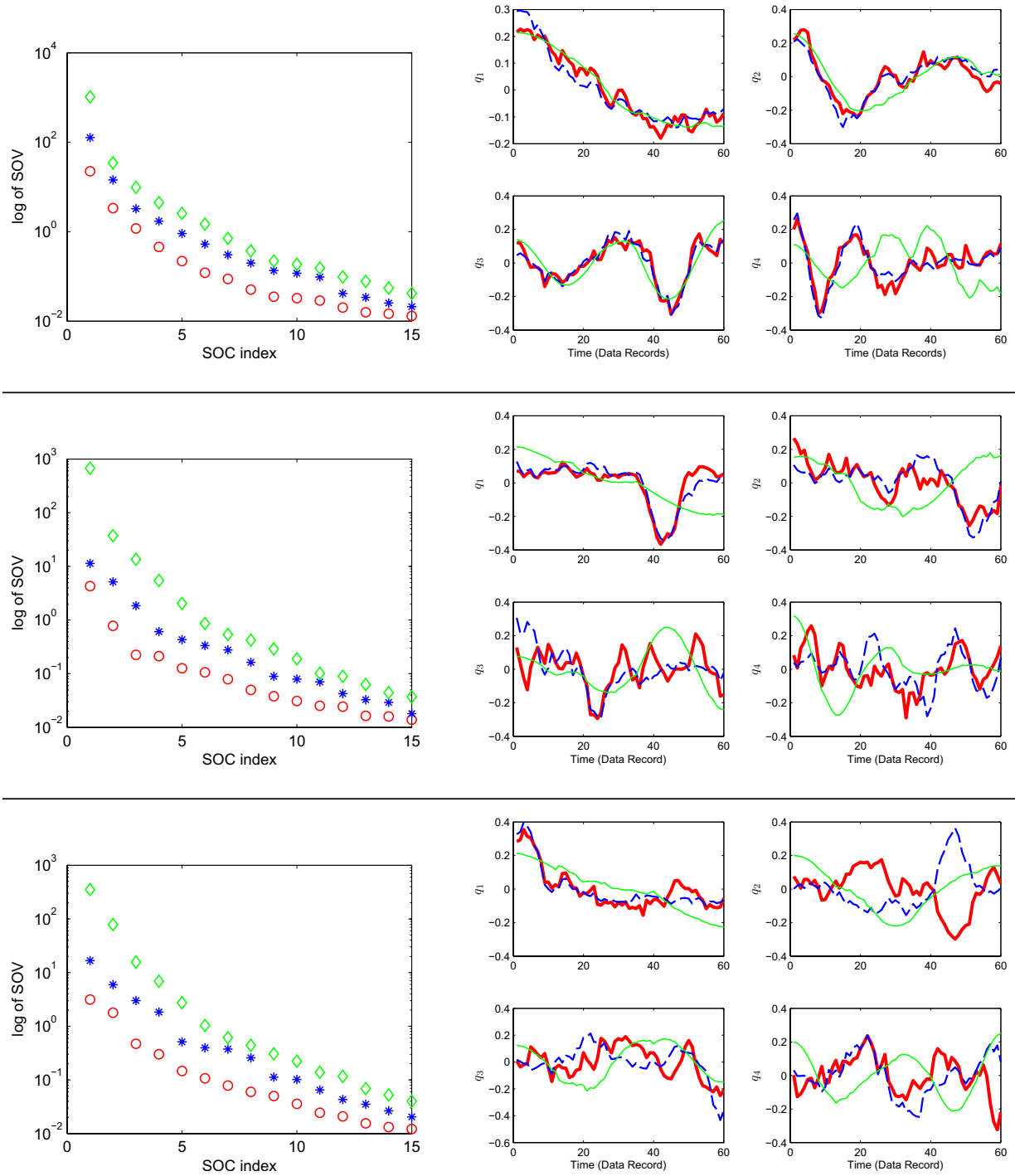

Fig. 4 Left plots: first 15 dominant linear (red ○), quadratic (blue *), and cubic (green ◇) SOVs for subject 6 elbow flexion/extension (top), humeral plane angle (middle), and humeral elevation angle (bottom). The corresponding first four dominant linear (thick red line), quadratic (dashed blue line), and cubic (thin green line) SOCs for subject 6 elbow flexion/extension (plots on the right).

least-squares sense. An ad hoc F-test ($p<0.05$) is used to tell how many SOCs are required to adequately describe the local muscle fatigue EMG trends. If the projections track the EMG well, meaning an R^2 value is close to 1, then there is a one-to-one map from the corresponding SOC space to the particular EMG space.

Figure 5 depicts the between subject variability in R^2 values of the SOC fits. Across all subjects and muscles, it is evident that the NSOD-based fits have consistently higher R^2 values compared with the linear SOD results, with cubic SOD fits showing the largest R^2 values. In addition, cubic coordinates also show a significant decrease in the variability of the quality of fits across all subjects. The most significant improvement in the quality of fit is seen in the humeral plane angle. For this angle, linear SOD fits need, on average, 15 SOCs to adequately track the local EMG trends. Using the NSOD analysis, this number of required SOCs is significantly reduced to just three to five coordinates for the quadratic and just three for the cubic. Similar improvements are observed for every angle. The best case scenario is that for the humeral elevation angle, only two nonlinear coordinates are needed to track the triceps muscle.

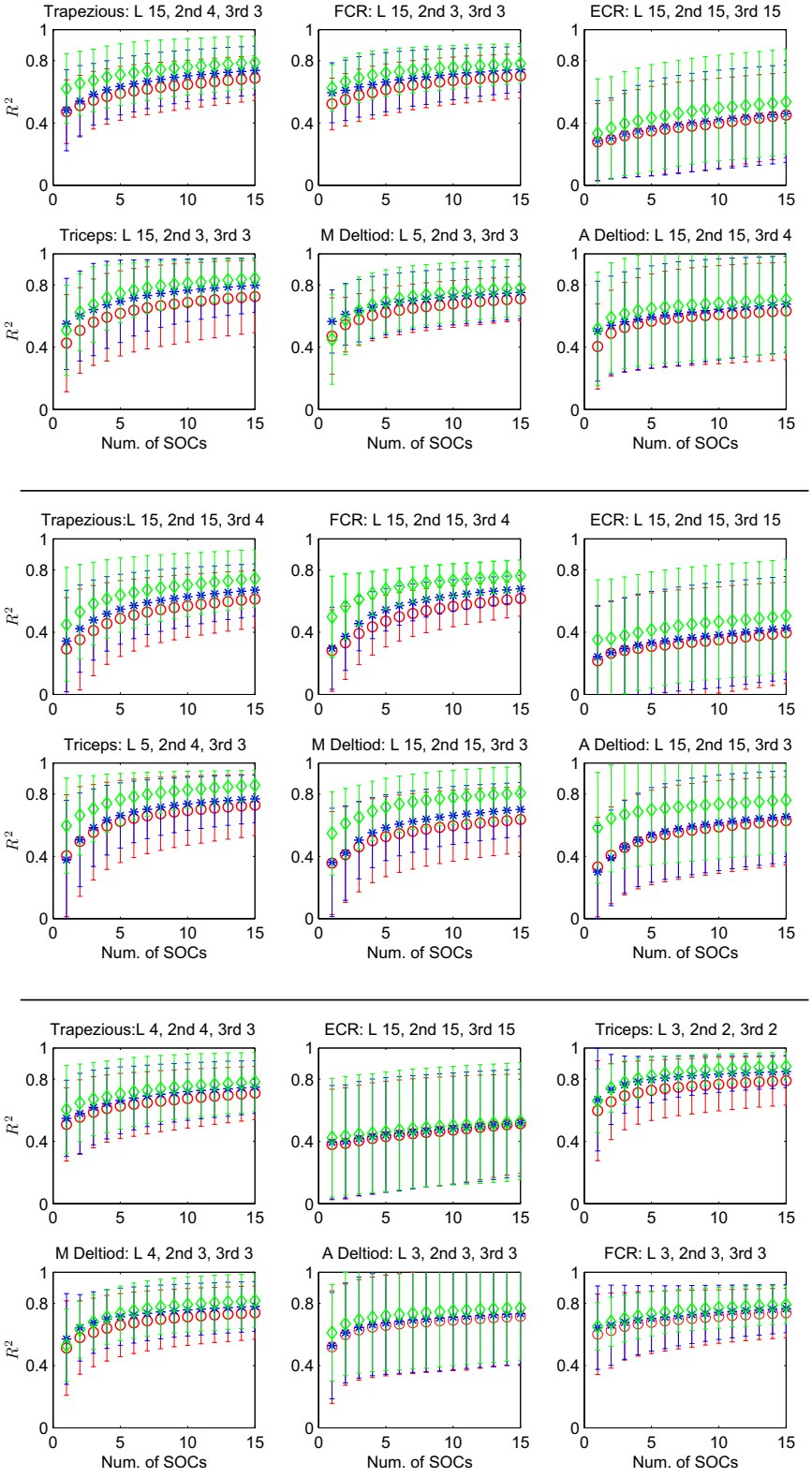

Fig. 5 Between subject variability in R^2 values for MNF trends for linear (red ○), quadratic (blue *), and cubic (green ◇) SOCs. Error bars represent one standard deviation from the mean of R^2. Elbow flexion/extension angle (top two rows), humeral plane angle (middle plots), and humeral elevation angle (bottom plots). Values on top of each plot indicate the number of SOCs needed to adequately track EMG trends.

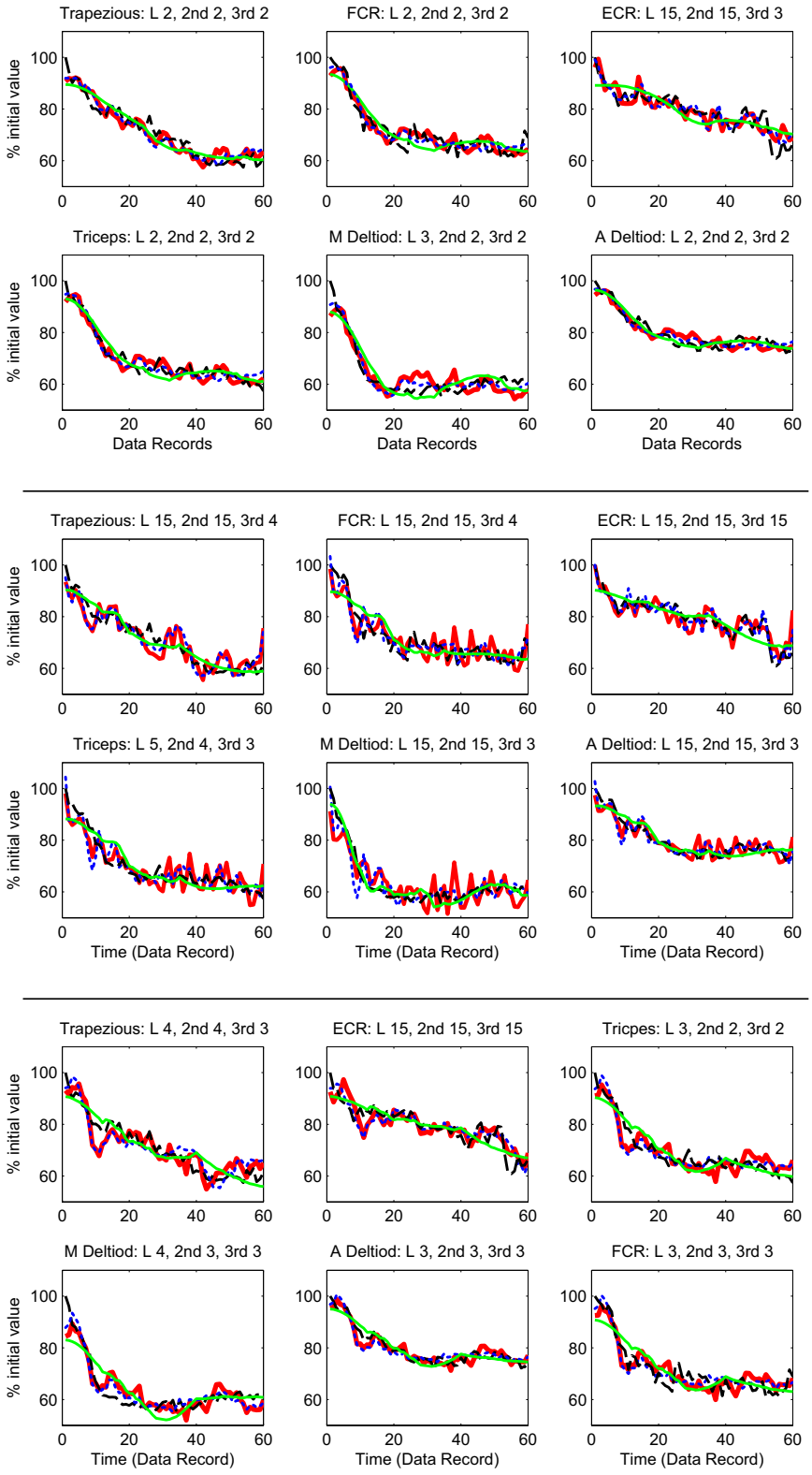

Fig. 6 Linear combinations of basic (thick red line), quadratic (dotted blue line), and cubic (thin green line) SOCs projections onto MNF (dashed black line) markers in a least squares sense for subject 6: (top plots) elbow flexion/extension angle (middle plots) humeral plane angle, and (bottom plots) humeral elevation angle

The corresponding projections of both linear and nonlinear SOCs onto the local EMG trends are shown to illustrate how well SOC fits match the actual EMG trends (Fig. 6). The number of SOCs in each projection is taken from the values indicated on the top of Figs. 5 and 6. The first thing to notice is how much smoother the nonlinear tracking is compared with the linear one in almost all cases, with cubic SOC fits being smoothest. Again, this relates to the improved degree of smoothness exhibited by the nonlinear SOCs. Also, we can see that the nonlinear fits more closely track the actual EMG trend while needing fewer coordinates.

6 Discussion

Plots in Fig. 4 show both linear and nonlinear SOD analyses of kinematic PSW features. Across all three kinematic angles displayed, increases in the order of SOD correspond to the increases in SOV magnitude and decreases in the local fluctuations of the corresponding SOCs. Since EMG-based muscle fatigue markers (Fig. 3) exhibit a generally slow variation in time, smoothest kinematic SOCs are expected to capture this information in a lower-dimensional manifold, which was conformed by analyzing the corresponding fits, as indicated in Fig. 5.

Figure 5 shows between-subject variability in R^2 values for the SOC-based fits to the EMG markers. Two important aspects of Fig. 5 give further validity to the nonlinear SOCs, providing more optimal coordinates to describe fatigue dynamics. First, R^2 values from nonlinear SOCs are larger for all three kinematic angles and muscle groups, cubic being the largest. This is an indication that for the same number of coordinates, nonlinear SOCs provide better approximation to EMG-based trends. Even if the number of linear SOCs is increased substantially, NSOD-based fits are still better. Second, there is a drastic decrease in the amount of SOCs that are needed to adequately track the EMG-based trends with the increase in the order of SOD. The elbow flexion/extension and humeral elevation angles show the smallest improvement, whereas the humeral plane angle shows the greatest improvement.

The improvements in the humeral plane angle goes from needing around 15 SOCs for adequate tracking to 4 quadratic and 3 cubic SOCs, or the dimensionality of tracking SOC manifold decreases by one order of magnitude. In the triceps muscle, elbow flexion/extension and humeral plain angles only need three nonlinear SOCs, and the humeral elevation angle needs two nonlinear SOCs. This means that for elbow flexion/extension and humeral plane angles we can represent the EMG by a three-dimensional manifold, and only a two-dimensional manifold is needed for the humeral elevation angle. If we used the linear SOCs, we would need, on the average, a 15-dimensional manifold to track or predict the fatigue dynamics, as indicated by the conventional EMG-based analysis.

Figure 6 shows both linear and nonlinear coordinates projected onto MNF EMG trends. The amount of SOCs in each projection is indicated on top of corresponding plots in Figs. 5 and 6. The results suggest that the cubic SOCs track the EMG trends with more precision and are closer to the actual trends. The linear SOC projections contain more high frequency information than the nonlinear ones, with cubic being the smoothest projection.

7 Conclusion

Current methodologies of tracking and predicting fatigue are either invasive or cumbersome. This makes them not realizable in the field. It was our intent to show that using noninvasive measurements of movement kinematics, nonlinear SOD of PSW features can identify more optimal smooth coordinates than its linear counterpart. This was demonstrated by performing a sawing experiment where ten healthy right-handed subjects performed a sawing motion by pushing a weighted handle back and forth until voluntary exhaustion. Three sets of joint kinematic angles were measured from the elbow, wrist, and shoulder, in addition to surface EMG recordings from nine different muscle groups. The SOD analysis indicates that the linear SOCs were contaminated with more high frequency content than the corresponding nonlinear coordinates for the same modal index. This resulted in considerably fewer nonlinear SOCs needed to reconstruct the muscle fatigue trend compared with the linear SOCs. The coefficient of determination R^2 values indicate roughly a 15-dimensional manifold in the linear SOD analysis is needed to reconstruct the traditional EMG-based local muscle fatigue indicators. However, utilizing nonlinear SOD, it was shown that a four- or five-dimensional manifold can capture the same information for quadratic SOCs, and two-dimensional reconstructions were possible using cubic SOD. Thus, nonlinear SOD extracts more optimal coordinates than linear SOD and, in doing so, reduces the required dimensionality by roughly one order of magnitude.

The results of this paper, in conjunction with Ref. [20], indicate that motion kinematic data can be used to track fatigue in local muscle groups. Tracking of fatigue in all these muscle groups can be accomplished using the same few nonlinear SOCs, effectively embedding all muscle fatigue dynamics in a fairly low-dimensional space. Therefore, one can speculate that low-dimensional dynamical models of fatigue utilizing kinematic data can be used to develop more robust training protocols and energy supplements or to predict muscle injuries. In turn, the development of these models can be guided and verified by the observed SOCs.

Acknowledgment

This study was supported by the National Institute of Biomedical Imaging and Bioengineering Grant No. 1R21EB003425-01A1. D.C. was also supported in part by the National Science Foundation Grant No. 0237792.

References

[1] Bigland-Ritchie, B., and Woods, J. J., 1984, "Changes in Muscle Contractile Properties and Neural Control During Human Muscular Fatigue," Muscle Nerve, **11**, pp. 251–279.
[2] DeLuca, C. J., 1984, "Myoelectrical Manifestations of Localized Muscular Fatigue in Humans," Crit. Rev. Biomed. Eng., **11**, pp. 251–279.
[3] Gandevia, S. C., 2001, "Spinal and Supraspinal Factors in Human Muscle Fatigue," Physiol. Rev., **81**, pp. 1725–1789.
[4] Torvik, V., Triantaphyllow, E., Liao, T., and Waly, S., 1999, "Predicting Muscle Fatigue via Electromyography: A Comparative Study," Proceedings of the 25th International Conference on Computers and Industrial Engineering, pp. 277–280.
[5] Brooks, G., Fahey, T., and White, T., 1996, *Exercise Physiology: Human Bioenergetics and Its Applications*, 2nd ed., Mayeld, Mountain View, CA.
[6] Febbraio, M., and Dancey, J., 1999, "Skeletal Muscle Energy Metabolism During Prolonged Fatiguing Exercise," J. Appl. Physiol., **87**, pp. 2341–2347.
[7] Beck, T. W., Housh, T. J., Johnson, G. O., Weir, J. P., Cramer, J. T., Coburn, J. W., and Malek, M. H., 2005, "Comparison of Fourier and Wavelet Transform Procedures for Examining the Mechanomyographic and Electromyographic Frequency Domain Responses During Fatiguing Isokinetic Muscle Actions of the Biceps Brachii," J. Electromyogr Kinesiol, **15**(2), pp. 190–199.
[8] Clancy, E. A., Farina, D., and Merletti, R., 2005, "Cross-Comparison of Time- and Frequency-Domain Methods for Monitoring the Myoelectric Signal During a Cyclic, Force-Varying, Fatiguing Hand-Grip Task," J. Electromyogr Kinesiol, **15**(3), pp. 256–265.
[9] MacIsaac, D., Parker, P., and Scott, R., 2001, "The Short-Time Fourier Transform and Muscle Fatigue Assessment in Dynamic Contractions," J. Electromyogr Kinesiol, **11**(6), pp. 439–449.
[10] Oka, H., 1996, "Estimation of Muscle Fatigue by Using EMG and Muscle Stiffness," 18th Annual International Conference of the IEEE Engineering in Medicine and Biology Society, Amsterdam.
[11] DeLuca, C., 1997, "The Use of Surface Electromyography in Biomechanics," J. Appl. Biomech., **13**, pp. 135–163.
[12] Selen, L. P. J., Beek, P. J., and van Dien, J. H., 2007, "Fatigue-Induced Changes of Impedance and Performance in Target Tracking," Exp. Brain Res., **181**, pp. 99–108.
[13] Farina, D., Fattorini, L., Felici, F., and Filligoi, G., 2002, "Nonlinear Surface EMG Analysis to Detect Changes of Motor Unit Conduction Velocity and Synchronization," J. Appl. Physiol., **93**, pp. 1753–1763.
[14] Arihara, M., and Sakamoto, K., 1999, "Contribution of Motor Unit Activity Enhanced by Acute Fatigue to Physiological Tremor," Electromyogr. Clin. Neurophysiol., **39**, pp. 235–247.
[15] Hunter, S. K., Critchlow, A., Shin, I.-S., and Enoka, R. M., 2004, "Fatigability of the Elbow Flexor Muscles for a Sustained Submaximal Contraction Is Similar in Men and Women Matched for Strength," J. Appl. Physiol., **96**, pp.

195–202.
[16] Chelidze, D., and Cusumano, J. P., 2006, "Phase Space Warping: Nonlinear Time Series Analysis for Slowly Drifting Systems," Philos. Trans. R. Soc. London, Ser. A, **364**, pp. 2495–2513.
[17] Dingwell, J. B., Napolitano, D. F., and Chelidze, D., 2007, "A Nonlinear Approach to Tracking Slow-Time-Scale Changes in Movement Kinematics," J. Biomech., **40**, pp. 1629–1634.
[18] Chatterjee, A., 2000, "An Introduction to the Proper Orthogonal Decomposition," Curr. Sci., **78**(7), pp. 808–817.
[19] Chelidze, D., and Zhou, W., 2006, "Smooth Orthogonal Decomposition Based Modal Analysis," J. Sound Vib., **292**(3–5), pp. 461–473.
[20] Song, M., Segala, D. B., Dingwell, J. B., and Chelidze, D., 2009, "Slow-Time Changes in Human Muscle Fatigue Are Fully Represented in Movement Kinematics," ASME J. Biomech. Eng., **131**, p. 021004.
[21] Segala, D., Chelidze, D., Adams, A., Schiman, J., Piscitelle, L., and Hasselquist, L., 2008, "Tracking Physiological Fatigue in Prolonged Load Carriage Walking Using Phase Space Warping and Smooth Orthogonal Decomposition," Proceedings of the IDETC/CIE 2008 ASME International Mechanical Engineering Congress and Exposition, Boston, MA, Oct. 31–Nov. 6.
[22] Segala, D., Gates, G., Dingwell, J., and Chelidze, D., 2009, "Smooth Orthogonal Decomposition Based Fatigue Trends Identified in Walking Warfighters and Gait Movements Representing Sawing Motion," Proceedings of the IDETC/CIE 2009 ASME International Mechanical Engineering Congress and Exposition, Lake Buena Vista, FL, Nov. 13–19.
[23] Segala, D., Gates, G., Dingwell, J., and Chelidze, D., 2009, "Dynamical Analysis of Sawing Motion Tracks Muscle Fatigue Evolution," Proceedings of the IDETC/CIE 2009 ASME IDETC Conference, San Diego, CA, Aug. 30–Sept. 2.
[24] Chelidze, D., and Liu, M., 2008, "Reconstructing Slow-Time Dynamics From Fast-Time Measurements," Philos. Trans. R. Soc. London, Ser. A, **366**, pp. 729–745.
[25] Sauer, T., Yorke, J. A., and Casdagli, M., 1991, "Embedology," J. Stat. Phys., **65**(3–4), pp. 579–616.
[26] Kennel, M., Brown, R., and Abarbanel, H., 1992, "Determining Embedding Dimension for Phase-Space Reconstruction Using a Geometrical Construction," Phys. Rev. A, **45**(6), pp. 3403–3411.
[27] Fraser, A., and Swinney, H., 1986, "Independent Coordinates for Strange Attractors From Mutual Information," Phys. Rev. A, **33**(2), pp. 1134–1140.
[28] Gates, D., and Dingwell, J., 2008, "Effects of Muscle Fatigue on Variability and Temporal Correlations in Movement Timing Errors," Exp. Brain Res., **187**, pp. 573–585.
[29] Veldpaus, F. E., Woltring, H. J., and Dortmans, L. J. M. G., 1988, "A Least-Squares Algorithm for the Equiform Transformation From Spatial Marker Co-Ordinates," J. Biomech., **21**, pp. 45–54.
[30] Schmidt, R., Disselhorst-Klug, C., Silny, J., and Rau, G., 1999, "A Marker-Based Measurement Procedure for Unconstrained Wrist and Elbow Motions," J. Biomech., **32**, pp. 615–621.
[31] Wu, G., van der Helm, F. C. T., Veeger, H. E. J., Makhsous, M., Van Roy, P., Anglin, C., Nagels, J., Karduna, A. R., McQuade, K., Wang, X., Werner, F. W., and Buchholz, B., 2005, "ISB Recommendation on Definitions of Joint Coordinate Systems of Various Joints for the Reporting of Human Joint Motion—Part II: Shoulder, Elbow, Wrist and Hand," J. Biomech., **38**, pp. 981–992.
[32] Hingtgen, B., McGuire, J., Wang, M., and Harris, G., 2006, "An Upper Extremity Kinematic Model for Evaluation of Hemiparetic Stroke," J. Biomech., **39**, pp. 681–688.
[33] Rao, S., Bontruger, E., Gronley, J., Newsam, C., and Perry, J., 1996, "Three-Dimensional Kinematics of Wheelchair Propulsion," IEEE Trans. Rehabil. Eng., **4**(3), pp. 152–160.
[34] Perotto, A., 2005, *Anatomical Guide for the Electromyographer*, Charles C. Thomas Publisher, LTD, Springfield, IL.